Spatially variable fault friction derived from dynamic modeling of aseismic afterslip due to the 2004 Parkfield earthquake

Shu-Hao Chang,[1,2] Jean-Philippe Avouac,[1] Sylvain Barbot,[1,3] and Jian-Cheng Lee[2]

[1] We investigate fault friction from dynamic modeling of fault slip prior to and following the M_w 6.0 earthquake which ruptured the Parkfield segment of the San Andreas Fault in 2004. The dynamic modeling assumes a purely rate-strengthening friction law, with a logarithmic dependency on sliding rate: $\mu = \mu_* + (a - b) \ln\left(\frac{v}{v_*}\right)$. The initial state of stress is explicitly taken into account, and afterslip is triggered by the stress change induced by the earthquake source model given a priori. We consider different initial stress states and two coseismic models, and invert for the other model parameters using a nonlinear inversion scheme. The model parameters include the reference friction μ_*, the friction rate dependency characterized by the quantity a-b, assumed to be either uniform or depth dependent. The model parameters are determined from fitting the transient postseismic geodetic signal measured at continuous GPS stations. Our study provides a view of frictional properties at the kilometers scale over the 0–15 km depth illuminated by the coseismic stress change induced by the Parkfield earthquake. The reference friction is estimated to be between 0.1 and 0.5. With independent a priori constraints on the amplitude of differential stress, the range of possible values narrows down to 0.1–0.17. The friction rate coefficient a-b is estimated to be $\sim 10^{-3} - 10^{-2}$ with a hint that it increases upward from about 1–3×10^{-3} at 3–7 km depth to about 4–7×10^{-3} at 0–1 km depth. It is remarkable that our results are consistent with frictional properties measured on rock samples recovered from the fault zone thanks to the San Andreas Fault Observatory at Depth experiment.

1. Introduction

[2] Slip on faults at seismogenic depth is thought to be largely governed by frictional processes [e.g., *Scholz*, 2002]. Fault frictional properties determine the level of shear stress during sliding and whether sliding is steady or unsteady [*Byerlee*, 1978; *Dieterich*, 1979; *Ruina*, 1983]. It has been shown that dynamic modeling of the seismic cycle on faults using friction laws established in the laboratory [e.g., *Dieterich*, 1979; *Marone*, 1998] can reproduce most aspects of the seismic cycle qualitatively [e.g., *Tse and Rice*, 1986] and even quantitatively when appropriate measurements of interseismic strain build up and coseismic strain release are available [*Barbot et al.*, 2012]. Constraining fault frictional properties is therefore a major objective of seismotectonic studies. The San Andreas Fault in California has received much attention in that regard, and its frictional strength has been the subject of a long-lasting debate. Mostly based on stress measurements in deep boreholes [e.g., *Scholz*, 2000; *Hickman et al.*, 2004], some authors have argued for a high friction of 0.5–0.8 close to the typical values measured in the laboratory on most common crustal rocks [e.g., *Byerlee*, 1978]. Other authors have argued for significantly smaller values ($\mu < 0.2$) mostly based on heat-flow data or on the orientation of principal horizontal stresses with respect to the fault strike [*Brune et al.*, 1969; *Lachenbuch and Sass*, 1980; *Mount and Suppe*, 1987; *Hardebeck and Hauksson*, 2001; *Provost and Houston*, 2001; *Hickman et al.*, 2004]. Fault friction properties can also be investigated from the observations of afterslip following large earthquakes [e.g., *Marone et al.*, 1991; *Linker and Rice*, 1997; *Hearn et al.*, 2002; *Miyazaki et al.*, 2004; *Perfettini and Avouac*, 2004, 2007; *Fukuda et al.*, 2009]. This is the approach taken in this study. In principle, the time evolution of afterslip can indeed provide constraints on the slip-rate dependency of friction on faults undergoing steady slip. This dependency is commonly characterized by the friction rate parameter $\frac{\partial \mu}{\partial \ln V}$, where μ is the friction coefficient and V is the sliding velocity. This quantity, which is often written as a-b in reference to rate-and-state friction laws [*Dieterich*, 1979; *Ruina*, 1983], is relevant because laboratory experiments at slow slip rates show a logarithmic dependency of friction on sliding rate. This approach has in

[1]Tectonics Observatory, Division of Geological and Planetary Sciences, California Institute of Technology, Pasadena, California, USA.
[2]Institute of Earth Sciences, Academia Sinica, Taipei, Taiwan.
[3]Division of Earth Sciences, Nanyang Technological University, Singapore.

Corresponding author: S.-H. Chang, Institute of Earth Sciences, Academia Sinica, Taipei 11529, Taiwan. (hao9702@earth.sinica.edu.tw)
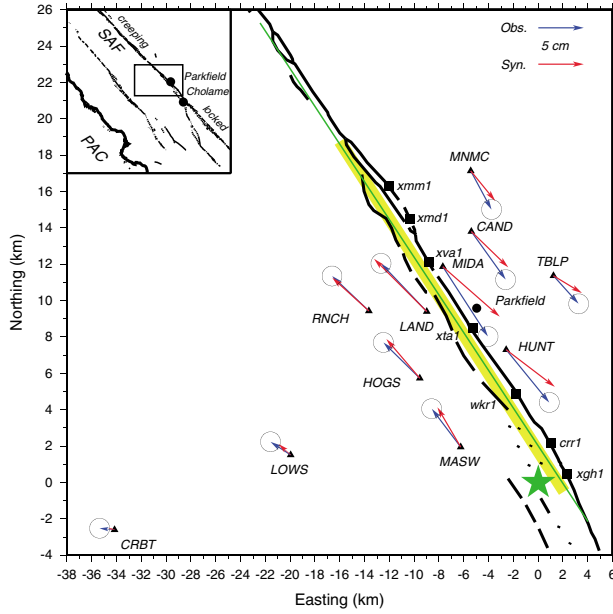
Figure 1. Observed and predicted postseismic displacements due to the M_w 6.0 earthquake of 2004 on the Parkfield segment of the San Andreas Fault. Inset shows location of the study area. Blue arrows with 2-σ uncertainties ellipses show cumulative postseismic displacements up to 548 days after the main shock derived from the SOPAC GPS time series. Red arrows show corresponding predicted displacements for the four layer velocity-strengthening model with the coseismic source Model B. Black line shows fault trace, and green line shows the location of the vertical planar fault model assumed in this study. Green star shows the epicenter of the 2004 Parkfield earthquake, and black squares show locations of creepmeters. The rupture extent of the 2004 earthquake is highlighted in yellow.

particular been applied to the analysis of postseismic relaxation following the 2004 Parkfield earthquake [*Johnson et al.*, 2006; *Barbot et al.*, 2009]. Interestingly, these two studies yielded widely different estimates of the friction rate parameter: *Johnson et al.* [2006] reported an estimate of 10^{-4}–10^{-3} (assuming an effective normal stress $\sigma_n = 50$ MPa); *Barbot et al.* [2009] obtained an estimate 1 order of magnitude larger of about 7×10^{-3} (assuming $\sigma_n = 100$ MPa). This type of modeling actually allows solving only for $\frac{\partial \mu}{\partial \ln V} \sigma_n$. Therefore, these two studies imply, respectively, $\frac{\partial \mu}{\partial \ln V} \sigma_n = 5 - 50$ kPa and $\frac{\partial \mu}{\partial \ln V} \sigma_n = 700$ kPa making the discrepancy even more obvious. The reason for this large discrepancy is unclear. In this article, we adopt a similar approach in that fault frictional properties are determined from the comparison of geodetic records with dynamic modeling of afterslip. We do not allow *a-b* to change with time as one purpose of the study is to evaluate whether the friction law we use succeeds at reproducing the temporal evolution of the surface deformation. However, we recognize that in reality fault frictional properties may vary substantially depending on the sliding velocity or other environmental parameters (temperature, fluid pressure) as has been observed in laboratory experiments [e.g., *Niemeijer and Spiers*, 2006]. The main differences between our study and the two previous studies are that (1) we solve for reference

friction, μ_*, and the preseismic stress which is assumed to drive secular interseismic slip; (2) we explore the possibility of solving for depth variations of the friction rate parameter as this parameter is thought to vary with depth either because of the effect of temperature or of lithification [e.g., *Marone*, 1998]; and (3) we use a more realistic, elastic model of coseismic slip of the Parkfield earthquake.

2. Overview of Seismotectonic Setting and Afterslip Following the Parkfield Earthquake

[3] The 2004 M_w 6.0 Parkfield earthquake ruptured a ~15 km long segment of the San Andreas Fault (Figure 1) which lies just south of the creeping segment of the San Andreas Fault. The fault is estimated to slip at a long-term geological rate of 26.2 +6.4/−4.3 mm/yr [*Toké et al.*, 2011] consistent with the slip rate derived from modeling interseismic geodetic strain [*Lisowski et al.*, 1991; *Murray et al.*, 2001]. This short segment lies between a 150 km long "creeping" segment to the North, where fault slip occurs mostly through aseismic steady sliding, and the 300 km long Cholame segment to the South, which last ruptured in 1857 during the M_w 7.9 Fort Tejon earthquake. Since 1881, five similar M_w ~6.0 earthquakes ruptured this fault segment 12 to 38 years apart [*Bakun and McEvilly*, 1984; *Bakun et al.*, 2005]. This regularity has prompted a significant monitoring effort after the 1966 earthquake. This effect has resulted in abundant information on background seismicity and secular deformation along that fault segment as well as coseismic and postseismic deformation associated with the 2004 event [e.g., *Bakun et al.*, 2005; *Stuart and Tullis*, 1995; *Murray et al.*, 2001; *Waldhauser et al.*, 2004] (Figure 1). This dataset provides an unprecedented opportunity to better resolve the frictional properties on the Parkfield section of the San Andreas Fault.

[4] It has already been shown that postseismic relaxation of the 2004 Parkfield earthquake was dominated by afterslip in the upper crust [e.g., *Freed*, 2007; *Johanson et al.*, 2006; *Langbein et al.*, 2006; *Murray and Langbein*, 2006; *Bruhat et al.*, 2011; *Johnson et al.*, 2006; *Barbot et al.*, 2009]. These studies all show that afterslip occurred predominantly on regions surrounding the fault patch that ruptured during the earthquake. Over the first year following the main shock, afterslip released a slip-potency (integral of slip over fault area) equivalent to 2 to 3 times the moment released during the coseismic phase and corresponding to a moment magnitude of about M_w 6.3. As mentioned before, the studies of *Johnson et al.* [2006] and *Barbot et al.* [2009] yielded quite different estimates of the friction rate parameter although they were based on similar data. These studies differ not only because *Johnson et al.* [2006] considered a rate-and-state friction law, while *Barbot et al.* [2009] assumed a purely rate-dependent friction law, but also because different coseismic models were used. A number of coseismic slip models have been determined [e.g., *Langbein et al.*, 2006; *Allmann and Shearer*, 2007; *Lengliné and Marsan*, 2009; *Bennington et al.*, 2011; *Bruhat et al.*, 2011; *Barbot et al.*, 2009, 2012; *Ziv*, 2012]. These models differ widely regarding the details of the seismic slip pattern, but they fall roughly into two main categories: the "geodetic" models that were derived from geodetic and remote-sensing data assuming a homogeneous half space model [e.g., *Langbein et al.*, 2006;
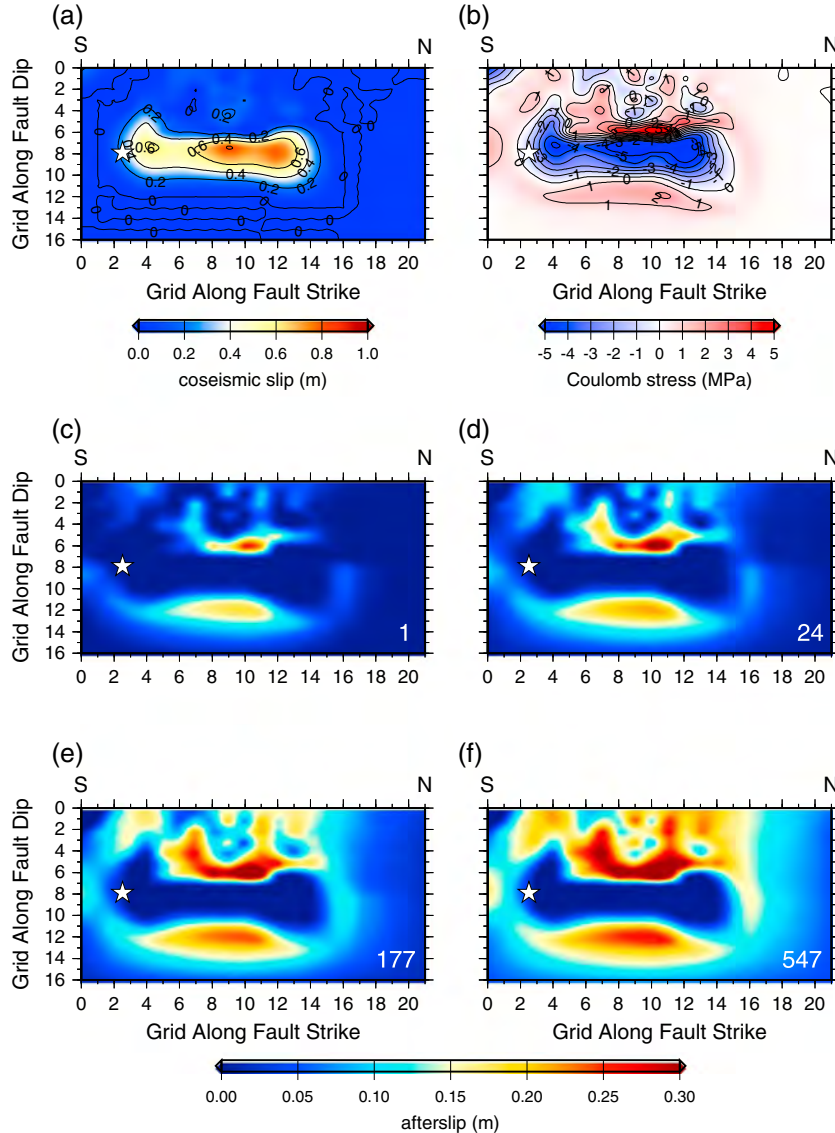
Figure 2. (a) Coseismic slip distribution and (b) the coseismic Coulomb failure stress changes on the fault plane of the 2004 Parkfield earthquake, corresponding to Model B, and (c–f) predicted postseismic slip over different time periods. The coseismic slip distribution shown in Figure 2a was determined from the inversion of GPS and InSAR data with a priori constraints derived from microseismicity and interseismic creep [*Barbot et al.*, 2012]. The preferred case of temporal variation of the afterslip predicted from dynamic modeling in Figures 2c–2f yields a reference friction $\mu_* = 0.17$, a depth variable rate dependency of friction (considering four layers with *a-b* values represented in Figures 5 and 6), and a vertical gradient of differential stress $\frac{d(\sigma_1 - \sigma_3)}{dz} = 10$ MPa/km. White numbers in Figures 2c–2f indicate number of days after the main shock (28 September 2004). The white star indicates the focus of the main shock.

Barbot et al., 2009] and the "seismological" models that were obtained from the inversion of accelerometrics records or tied to aftershock locations [e.g., *Ziv*, 2012; *Bennington et al.*, 2011; *Allmann and Shearer*, 2007], which either explicitly or implicitly (through the aftershocks location) take a more realistic elastic structure of the crust into account. All these models indicate a rupture depth range between 3 and 10 km, but the bulk of the moment is released at shallower depth, typically between 2.5 and 7 km according to "geodetic" models. In the "seismological" models, the bulk of the moment is released at depth typically between 6 and 10 km.

3. Model Assumptions and Data

[5] In this study, we determine the parameters of a dynamic afterslip model in order to best fit postseismic displacements recorded at GPS stations as well as surface fault slip recorded at creepmeters over 548 days following the 2004 Parkfield earthquake (Figures 1–3). We use time series of daily positions measured at 11 continuous GPS stations [*Langbein and Bock*, 2004] determined by the Scripps Orbit and Permanent Array Center after common mode noise filtering [http://sopac.ucsd.edu/]. The noise reduction methodology is presented by *Wdowinski et al.* [1997]. The postseismic signal is isolated
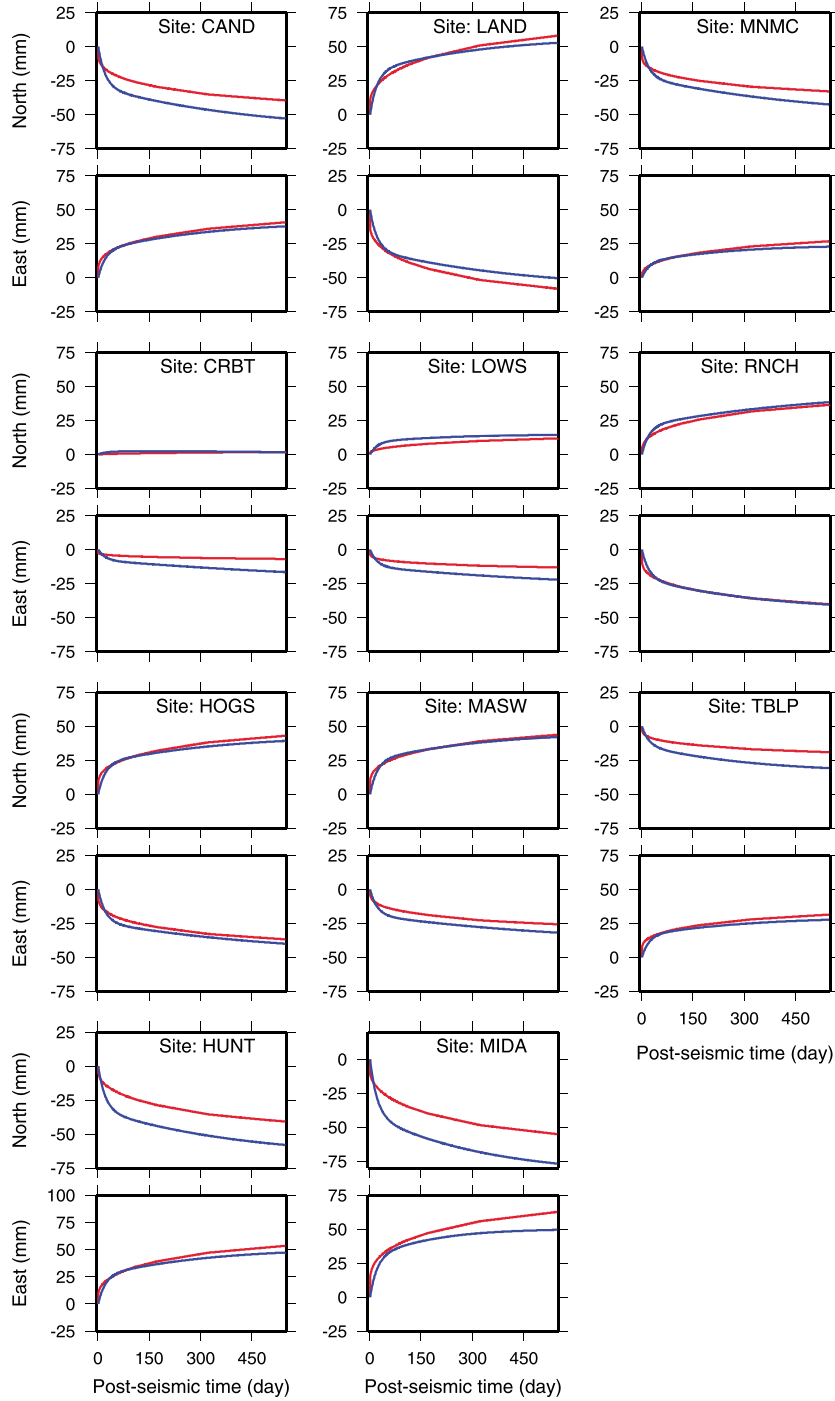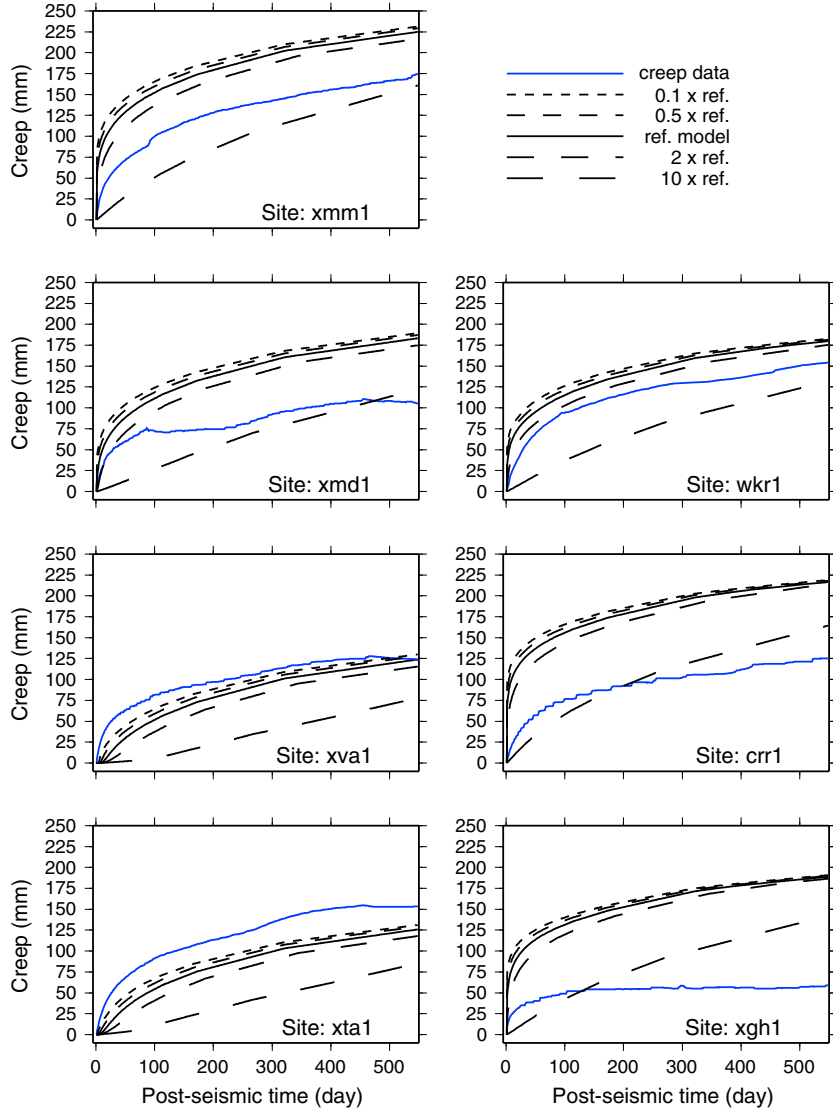
Figure 3. Comparisons between the predicted (red) and observed (blue) postseismic displacements at all the 11 continuous recording GPS stations in both the North and East components. The predicted displacements derived from dynamic modeling in the preferred case, which yields a reference friction $\mu_* = 0.17$, a depth variable rate-dependency of friction (considering four layers with a-b values represented in Figures 5 and 6), and a vertical gradient of differential stress $\frac{d(\sigma_1 - \sigma_3)}{dz} = 10$ MPa/km.

by substracting the interseismic linear trend from each time series [*Barbot et al.*, 2009]. The same procedure is applied to the model predictions (the synthetic linear trend predicted by the model is also removed). The reason for comparing observed and predicted transients is that our model does not include all the sources of deformation that may contribute to the interseismic displacements measured at those stations

(e.g., the aseismic creep beneath the segments of the SAF to the North and South of the Parkfield segment). By contrast, it is probably correct to assume that all the sources of transient deformation are mostly related to afterslip following the earthquake, as assumed in our modeling.

[6] We also use creepmeter data measured at seven stations [*Langbein et al.*, 2006] which span the 15 km long area that

4

Figure 4. Comparisons between the model-predicted postseismic displacements and those observed from seven creepmeters. Blue line shows fault right-lateral slip displacements measured from creepmeters along the Parkfield fault segment. Black continuous line shows displacement predicted from dynamic modeling in the preferred case with a reference friction $\mu_* = 0.17$, a depth variable rate dependency of friction (considering four layers with $a\text{-}b$ values represented in Figures 5 and 6), and a vertical gradient of differential stress $\frac{\mathrm{d}(\sigma_1 - \sigma_3)}{\mathrm{d}z} = 10$ MPa/km. The value of $a\text{-}b$ at the shallowest depth is 6.5×10^{-3} for this reference model. Different kinds of dashed lines show different model predictions when this value is varied within a factor of 10.

ruptured during the earthquake (Figure 1). The data show a clear rapid aseismic transient slip after the earthquake (Figure 4). The variability from site to site suggests significant along strike lateral variations of the shallow mechanical properties. It should be noted that several fault strands probably exist so that the creepmeters might capture only a fraction of the total signal across the fault [*Johanson et al.*, 2006; *Barbot et al.*, 2009]. For these reasons, these data are not used in our inversions but are only used to compare with the predictions from our best-fitting models. We thus use them as a posteriori tests of our model and to assess the spatial variability of fault frictional properties at a scale smaller than the resolution of the GPS data inversion.

[7] We assume that afterslip results from frictional sliding on the same fault plane that ruptured during the earthquake and

that the fault obeys a purely rate-strengthening friction law, equivalent to the steady state frictional regime for a rate-and-state friction law derived from laboratory experiments [*Ruina*, 1983; *Dieterich*, 1979]. The complete set of equations, with the aging form of the state evolution law, writes

$$\mu(V, \theta) = \mu_* + a \ln\left[\frac{V(t)}{V_*}\right] + b \ln\left[\frac{\theta(t)}{\theta_*}\right], \qquad (1)$$

$$\frac{\mathrm{d}\theta}{\mathrm{d}t} = 1 - \frac{V\theta}{d_c}, \qquad (2)$$

where V is the rate of fault slip; τ and σ represent the shear and effective normal stresses on the fault plane, respectively; μ_* is the friction coefficient under reference slip rate V_*; $\theta(t)$ and θ_* are state variables at time t and reference state, respectively;

and a, b, and d_c are empirical constants. In the steady state regime, this friction law is purely rate dependent, yielding

$$\tau = \sigma\mu_* + \sigma(a-b)\ln\left(\frac{V}{V_*}\right). \qquad (3)$$

[8] The friction rate dependency is then characterized by the rate parameter $\frac{\partial\mu}{\partial\ln V} = a - b$. When $a - b > 0$, friction is rate strengthening promoting aseismic slip. A fault patch obeying such a law and submitted to a constant stress would creep at a constant interseismic slip rate. If the stress level changes abruptly, say due to a nearby earthquake, a transient variation of slip rate is induced causing afterslip [*Marone et al.*, 1991].

[9] The time evolution of afterslip expected from rate-and-sate friction (equations (1) and (2)) or purely rate-strengthening friction in steady state (equation (3)) differs from each other only during an initial transient phase of adjustment of the state variable. During this transient phase, postseismic sliding rate should increase from an interseismic background value of $V_0\exp(\Delta\tau/a\sigma)$ to a value of $V_0\exp\left(\frac{\Delta\tau}{(a-b)\sigma}\right)$ and should decay later on as $1/t$ [*Perfettini and Avouac*, 2007; *Perfettini and Ampuero*, 2008]. The transient phase associated with the time needed for the state variable to fall back to close to the steady state value is probably very short, less than a few hours or even shorter [*Fukuda et al.*, 2009]. The daily geodetic data used in this study show only the $1/t$ decay phase, so that it is probably justified to assume steady state.

[10] The approach adopted in this study, as well as in the previous studies of *Johnson et al.* [2006] and *Barbot et al.* [2009], relies on the principle that if the coseismic stress change is known, the dependency of friction on sliding rate determines the afterslip response of the fault. We show in the following section that the preseismic frictional stress on the fault can be estimated in addition, providing constraints on the absolute value of the friction coefficient.

[11] One of the key elements of this approach is the choice of the coseismic slip model used to compute coseismic stress changes. For the purpose of this study, we considered two models, each representative of the "geodetic" and "seismological" categories: (1) Model A was derived by *Bruhat et al.* [2011] based on geodetic and InSAR data, and (2) Model B by *Barbot et al.* [2012] additionally used microseismicity distribution as an a priori constraint on the seismic slip distribution. Model A shows two asperities. The main asperity is about 6 km long and spans a depth range between 3 and 8 km with a maximum slip of 0.6 m (Figure A2). Model B has only one main relatively narrow and deeper asperity, about 10 km long, at a depth between 5 and 10 km (Figure 2). The maximum slip in this model is 0.7 m. The two models assume the same vertical planar fault striking 316° and show nearly pure right-lateral strike slip. Model B turned out to yield better results and is the one used in the Figures of the main text. The results obtained with Model A are given in the Appendices and used to estimate the sensitivity of our results to the assumed coseismic slip model.

4. Model Implementation and Inversion Technique

[12] We assume that afterslip following the 2004 Parkfield earthquake resulted from stress-driven frictional slip obeying the rate-strengthening friction law (equation (3)). Afterslip is assumed to occur on a planar fault surface which also contains the coseismic rupture. We consider a NW-striking (azimuth 316°) vertical fault 40 km long along strike and 15 km deep along dip. We further divided this fault plane into 300 subfaults (20 × 15), each with 2 km long along strike and 1 km deep along dip. We first assume that friction is rate strengthening $(a-b > 0)$ everywhere on the fault plane. This assumption ignores that some fractions of the fault areas that ruptured during the main shock and aftershocks must be rate weakening and, as such, did not contribute to afterslip. In a second step, we present results obtained assuming that afterslip is penalized within the rupture area. This test highlights the influence and possible bias introduced by the rate-weakening patches which remained locked during postseismic relaxation

[13] In principle, dynamic modeling of afterslip requires some knowledge of the preseismic stresses acting on the fault plane in addition to the stress change induced by coseismic deformation. In previous studies of dynamic modeling of afterslip, it was assumed (although not always explicitly) that coseismic slip and afterslip induce small perturbations of the preseismic stress and that the preseismic stress explains interseismic creep rates. With these assumptions, it is justified to analyze only the transient postseismic evolution of slip rate (after correcting the geodetic time series for the preearthquake secular rates) based on equation (3) rewritten as

$$\Delta CFF = \Delta\tau - \mu_*\Delta\sigma = \sigma(a-b)\ln\left(\frac{V}{V_*}\right), \qquad (4)$$

where ΔCFF stands for the so-called Coulomb stress change. Here, we relax that assumption as it does not need to be valid given the possible low preseismic stresses on the SAF. One advantage of our approach is that it makes it possible to determine the best-fitting preseismic stress and check whether the preseismic sliding rate, computed using the preseismic stress and the friction parameters derived from the afterslip modeling, is consistent with independent estimates of that quantity (i. e., $\sim$ 22–32 mm/yr) [*Lisowski et al.*, 1991; *Murray et al.*, 2001; *Toké et al.*, 2011].

[14] The shear stress, $\tau(i,t)$, and normal stress, $\sigma(i,t)$, on any fault patch i at time t can be written as

$$\tau(i,t) = \tau_0(i) + \Delta\tau_{\text{eq}}(i) + \Delta\tau_{\text{creep}}(i,t) \qquad (5)$$

$$\sigma(i,t) = \sigma_0(i) + \Delta\sigma_{\text{eq}}(i) + \Delta\sigma_{\text{creep}}(i,t), \qquad (6)$$

where $\tau_0(i)$ and $\sigma_0(i)$ are the initial shear and effective normal stresses; $\Delta\tau_{\text{eq}}(i)$ and $\Delta\sigma_{\text{eq}}(i)$ are the coseismic shear and effective normal stress changes induced by the earthquake; and $\Delta\tau_{\text{creep}}(i,t)$ and $\Delta\sigma_{\text{creep}}(i,t)$ are the shear and effective normal stress changes due to the time-evolution of afterslip rate, respectively. We thus need to estimate the initial shear and effective normal stresses acting on the fault, prior to the 2004 Parkfield earthquake. We assume that it is the resultant of a regional stress tensor, which only varies with depth. Based on the regional stress tensor inversion of *Provost and Houston* [2001], we assume that the intermediate principal stress $\sigma_2(i)$ is vertical, that the stress ratio of $\frac{\sigma_2-\sigma_3}{\sigma_1-\sigma_3} = 0.5$, and that the maximum principal horizontal stress $\sigma_1(i)$ strikes N25°E, i.e., at an angle of 69° relative to the surface trace of

the San Andreas Fault. This is also approximately the same stress orientation measured at the bottom of the San Andreas Fault Observatory at Depth (SAFOD) pilot hole at a depth of 2–2.2 km [*Hickman and Zoback*, 2004]. We additionally assume that the vertical stress increases linearly with depth assuming an average rock density $\rho = 2670$ kg m^{-3}. The intermediate effective principal stress is then equal to $\sigma'_2(i) = \rho g z(i)(1 - \lambda)$ where $g = 9.8$ m s^{-2} is the gravity, $z(i)$ is the depth of the subfault i, and λ is the pore pressure ratio. The differential stress $\sigma_1 - \sigma_3$ is assumed to increase linearly with depth. We test a relatively broad range of values since these stress magnitudes are poorly constrained.

[15] The initial shear and effective normal stresses $\tau_0(i)$ and $\sigma_0(i)$ depend on the principal stresses (with the convention that normal stress is positive in compression) $\sigma_1 > \sigma_2 > \sigma_3$ according to

$$\tau_0(i) = \frac{1}{2}[\sigma_1(i) - \sigma_3(i)]\sin 2\psi, \tag{7}$$

$$\sigma_0(i) = \frac{1}{2}[\sigma_1(i) + \sigma_3(i)] + \frac{1}{2}[\sigma_1(i) - \sigma_3(i)]\cos 2\psi, \tag{8}$$

where $\psi = 21°$ based on *Provost and Houston* [2001].

[16] The afterslip rake is determined assuming that slip is parallel to the shear stress acting on the fault. To simplify the computation and save on the computational cost, we assume that rake changes induced by shear stress changes during afterslip can be neglected.

[17] Stress changes due to coseismic slip and afterslip are calculated based on the semi-analytical solution of *Okada* [1992] for a dislocation in an elastic half-space. The shear modulus is taken to be 30 GPa, and the Poisson coefficient is chosen to be $\nu = 0.25$

[18] The stress changes due to afterslip are computed according to

$$\Delta\tau_{\text{creep}}(i,t) = \sum_{j=1}^{n} K_s(i,j)[u(j,t) - V_{pl}t], i = 1, n \tag{9}$$

$$\Delta\sigma_{\text{creep}}(i,t) = \sum_{j=1}^{n} K_n(i,j)[u(j,t) - V_{pl}t], i = 1, n \tag{10}$$

where $u(j,t)$ is the cumulative displacement of subfault j at time t, V_{pl} is the loading velocity due to slip on the downdip continuation of the fault, and K_s and K_n are the elastic kernels for the shear and effective normal stress changes induced by a unit slip on the subfault j in a given rake direction. We calculate the elastic kernels also by employing the analytical solution of *Okada* [1992].

[19] Combining equations (3)–(6), we get

$$V(i,t) = V_* \exp\left\{\frac{CFF_0(i) + \Delta CFF_{\text{eq}}(i) + \Delta CFF_{\text{creep}}(i,t)}{(a-b)[\sigma_0(i) + \Delta\sigma_{\text{eq}}(i) + \Delta\sigma_{\text{creep}}(i,t)]}\right\}, \tag{11}$$

where $V(i,t)$ is the slip rate of subfault i at time t, $CFF_0(i) = \tau_0(i) - \mu_*\sigma_0(i)$ is the initial Coulomb stress where μ_* denotes the friction coefficient at reference slip velocity V_*, and $\Delta CFF_{\text{eq}}(i) = \Delta\tau_{\text{eq}}(i) - \mu_*\Delta\sigma_{\text{eq}}(i)$ and $\Delta CFF_{\text{creep}}(i,t) = \Delta\tau_{\text{creep}}(i,t) - \mu_*\Delta\sigma_{\text{creep}}(i,t)$ are the Coulomb stress changes caused

by coseismic rupture and afterslip, respectively. The slip velocity prior to the earthquake is then

$$V_0(i) = V_* \exp\left[\frac{CFF_0(i)}{(a-b)\sigma_0(i)}\right]. \tag{12}$$

[20] We solve equation (11) with an implicit finite-difference method, such that

$$u_j^{i+1} = u_j^i + \Delta t V_* \exp\left\{\frac{CFF_{0j} + \Delta CFF_{\text{eq}j} + \Delta CFF_{\text{creep}j}^i}{(a-b)[\sigma_{0j} + \Delta\sigma_{\text{eq}j} + \Delta\sigma_{\text{creep}}^i]}\right\}, \tag{13}$$

where u_j^i denotes the cumulative displacement at the center of the subfault j at time step i. In this study, the time interval Δt is restricted to be less than 1 day, and the corresponding slip increment is less than 1 mm.

[21] In reality, slip on the modeled fault is not the only source of geodetic displacements measured at the various stations. For example, slip occurring along the downdip continuation of the fault must also contribute. We assume that these other sources of deformation are stationary so that they contribute only to the secular rate measured at these stations. So, we compare the transient time evolution of slip rate from the detrended GPS time series, using the secular rates determined by *Barbot et al.* [2009], with the transient time evolution of sliding rate predicted by our model:

$$\Delta V(i,t) = V_* \exp\left\{\frac{CFF_0(i) + \Delta CFF_{\text{eq}}(i) + \Delta CFF_{\text{creep}}(i,t)}{(a-b)[\sigma_0(i) + \Delta\sigma_{\text{eq}}(i) + \Delta\sigma_{\text{creep}}(i,t)]}\right\}$$
$$- V_* \exp\left[\frac{CFF_0(i)}{(a-b)\sigma_0(i)}\right]. \tag{14}$$

[22] We assume that the pore pressure ratio is hydrostatic ($\lambda = 0.4$) and the value of V_* is chosen to be 30 mm/yr, i.e., equal to the estimated long term slip rate. We vary $d(\sigma_1 - \sigma_3)/dz$ between 5 and 50 MPa/km. For each value of the stress gradient, the optimal values of a-b and μ_* are determined using the Neighborhood Algorithm (NA) of *Sambridge* [1999]. The range of model frictional parameters explored in the inversions is 0.0005 to 0.02 for a-b and 0.1 to 0.85 for μ_*. The minimized cost function is the root-mean-square (RMS) of the misfit between the detrended observed and modeled (equation (14)) surface displacement. For comparison, the nominal uncertainties of the measurements on the daily horizontal East and North GPS positions are about 5 mm on average. We do not use the vertical displacements in this study, because the detrended vertical displacements are negligible compared to the uncertainties.

[23] In the inversion, we first consider uniform frictional properties. In this case, only two parameters are determined, μ_* and a-b.

[24] In the case where a-b is allowed to vary with depth, we started with a larger number of layers (arbitrarily chosen to 12) and then combined the layers by trial and errors to limit trade-offs. We found that four layers was a good compromise to capture the depth variations needed to improve the fit without introducing too many parameters. The layers are thicker at depth than near the surface to account for the resolution

Table 1. Modeled Parameters With the Homogenous *a-b*

| Parameters	Model A					Model B					
$\frac{\partial(\sigma_1-\sigma_3)}{\partial z}$ (MPa/km)	10	20	30	40	50	5	10	20	30	40	50
μ^*	0.16	0.28	0.39	0.43	0.48	0.096	0.17	0.28	0.39	0.43	0.48
a-b ($\times 10^{-3}$)	5.2	4.3	3.8	3.3	2.9	2.3	2.0	1.7	1.5	1.3	1.2
RMS (mm)	7.37	7.36	7.35	7.34	7.33	6.13	6.14	6.14	6.15	6.15	6.16
V_0 (mm/yr)	43.2	42.0	43.4	47.2	46.1	27.1	26.8	26.8	26.6	26.6	27.1
M_0 ($\times 10^{18}$ N m)	2.3	2.3	2.3	2.3	2.3	1.9	1.9	1.9	1.9	1.9	1.9
M_w	6.21	6.21	6.21	6.21	6.21	6.15	6.15	6.15	6.15	6.15	6.15

of the inversion which worsens with depth. Only *a-b* varies. As μ_* is assumed to be uniform, the number of model parameters increases to 5. The layers are thicker at depth than near the surface to account for the better near surface resolution of the inversion. When the number of layers is increased beyond 4, the inversion becomes unstable because of the trade-offs among the parameters of adjacent layers. The NA inversion for these five parameters is run with 200 samples at the first iteration and 20 samples at each following iteration, which we run for up to a maximum of 5000 iterations. Computations were run on a supercomputer PANGU available at Caltech (http://citerra.gps.caltech.edu/).

5. Results

[25] Figures 1–4 show the predictions of one particular model, which was found to fit the postseismic transient displacements as well as the preseismic data satisfactorily and some other a priori constraints as discussed below. The various dynamic models of afterslip obtained from our modeling all predict a zone of afterslip fringing the coseismic rupture which later on spreads with time as afterslip rates relax (Figure 2). The relative amplitude of afterslip occurring downdip and updip of the coseismic rupture and the associated characteristic decay times varies depending on the assumed coseismic model (the depth is key as it determines the normal stresses acting on the fault) and depth variations of stress and frictional properties. Our inversions actually yield a suite of possible models which all fit the transient postseismic displacements relatively well with residuals RMS better than 8 mm which is of the order of the typical 1-σ uncertainties assigned to daily GPS solutions.

[26] The results obtained assuming uniform frictional properties are listed in Table 1. The postseismic transient displacements can be fitted about equally well with either Model A or B as the input coseismic slip distributions. There is a strong trade-off between the vertical gradient of differential stress $\frac{d(\sigma_1-\sigma_3)}{dz}$, the reference friction μ_*, and *a-b* (Table 1). According to equation (14), the relative impact of a given coseismic Coulomb stress change is enhanced if a lower differential stress gradient is assumed while all other parameters are held constant. In order to compensate this effect, either μ_* needs to be reduced or *a-b* increased. There is in fact an optimal change in the reference friction μ_* and in *a-b* to maintain a good fit with the observations: the ratio $\frac{(a-b)\frac{d(\sigma_1-\sigma_3)}{dz}}{\mu_*}$ has to be kept approximately constant. There exists therefore a broad range of models which yield similar fits to the geodetic data. Given the broad range of possible stress

gradients considered, we obtain a relatively broad range of acceptable values for μ_* between 0.1 and 0.48. However, the major trade-off is between μ_* and $\frac{d(\sigma_1-\sigma_3)}{dz}$ so that when
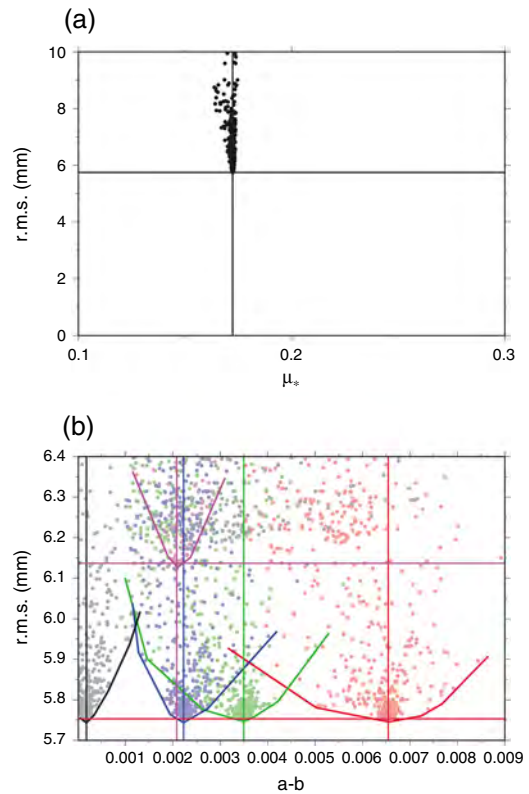
Figure 5. Results obtained from the inversion of the GPS times series of postseismic displacements using the Neighborhood Algorithm (NA). The plots show the root-mean-square (RMS) of the residuals computed for the various models tested during the convergence of the NA inversion as function of the (a) static friction coefficient, μ_*, and (b) rate-dependency coefficient, *a-b*. These are results from coseismic slip Model B with $\frac{d(\sigma_1-\sigma_3)}{dz} = 10$ MPa/km and either a uniform value of *a-b* or a four-layer model. In Figure 5a, the black dots represent the RMS values for the various tested models. In Figure 5b, the pink dots show RMS values for the homogeneous *a-b* models. The RMS values for the four *a-b* of the layered model from shallow to deep are denoted by red, green, blue, and black dots. We also use colored vertical lines to indicate the values of *a-b* for the best fitting model, and the brown horizontal line indicates the corresponding minimum RMS.

Table 2. Modeled Parameters With the Depth Varying a-b[a]

Parameters	Model A					Model B					
$\frac{\partial(\sigma_1-\sigma_3)}{\partial z}$ (MPa/km)	10	20	30	40	50	5	**10**	20	30	40	50
μ^*	0.16	0.28	0.37	0.43	0.48	0.095	**0.17**	0.28	0.39	0.43	0.48
a-b ($\times 10^{-3}$)			Figure A4						Figure 6		
RMS (mm)	7.04	7.00	6.94	6.88	6.86	5.76	**5.75**	6.06	6.05	6.06	6.06
V_0 (mm/yr)	79.6	79.4	80.8	81.6	81.7	28.5	**28.3**	30.8	31.0	30.5	30.4
M_0 ($\times 10^{18}$ N m)	2.2	2.2	2.2	2.3	2.2	2.1	**2.1**	1.7	1.7	1.7	1.7
M_w	6.20	6.20	6.20	6.20	6.20	6.19	**6.19**	6.12	6.13	6.12	6.12

[a]The Model B with vertical differential stress gradient of 10 MPa/km (in bold) is the preferred model in this study.

the stress gradient is fixed, the reference friction, μ_*, is quite tightly constrained (Figure 5a). The rate-dependency coefficient a-b is then constrained to a relatively narrow range: 2.9–5.2×10^{-3} with Model A and 1.2–2.0×10^{-3} with Model B. Despite the trade-offs among the model parameters, all acceptable models yield similar values of cumulated moment M_0 of 1.9 to 2.3×10^{18} N m (equivalent to a moment magnitude M_w of 6.2) corresponding to about 2–3 times the moment released coseismically.

[27] The interseismic creep rate (the rate at which the fault creeps given the preseismic stress and the fault frictional properties) is of the order of 43 to 47 mm/yr with Model A and 27 mm/yr with Model B. This rate is to be compared with the rate of 22–32 mm/yr derived from interseismic geodetic data and/or geological studies [*Lisowski et al.*, 1991; *Murray et al.*, 2001; *Toké et al.*, 2011]. Model B is therefore favored. In addition, Model B fits the postseismic time series slightly better, yielding a RMS of 6.15 mm compared to 7.3 mm with Model A.

[28] The results obtained allowing for depth variations of frictional properties are listed in Table 2. We considered four depth ranges each characterized by a single value of a-b. The time series of postseismic displacements are fitted slightly better than with the homogenous model, yielding RMS values of about 6.9 mm for Model A and 5.75 mm for Model B (Table 2). Estimated values of the reference friction coefficient μ_* are identical to those obtained in the previous inversions. We find again that Model B yields a somewhat better fit to the postseismic data and, more importantly, predicts an interseismic creep rate (28 mm/yr) in good agreement with the long-term slip rate on the fault. By contrast, we get values between 79 and 82 mm/yr with Model A. Model B is again found to reconcile the interseismic and postseismic observations better. All the acceptable models predict that afterslip over the 548 days covered by the dataset released a moment between 1.7 and 2.1×10^{18} N m, about equal to the moment derived assuming uniform friction rate dependency. So the estimation of that quantity is quite robust.

[29] The improvement of the four-layer model over the uniform model is significant at the 81% confidence level according to the statistical F test. We note that all models yield a similar range of values of a-b. The depth variations of a-b obtained for the various models show systematic similarities but some differences as well (Figures 6 and A4). A probably robust feature is that a-b is systematically largest in layer 1 (0–1 km depth) than in layers 2 and 3 (1–3 km and 3–7 km depth). Based on the coseismic slip Model B, the value of a-b is estimated to be about 4–7×10^{-3} for layer

1 and 2–4×10^{-3} for layer 2. All results with coseismic slip Model B show somewhat smaller values for layer 3 (3–7 km), where it is estimated to be 1–3×10^{-3}. The estimates for layer 4 (depth > 7 km) vary widely. Relatively large values of 6–9×10^{-3} are inferred for higher stress gradients (> 20 MPa/km), while relatively small values are obtained with lower stress gradients (≤ 10 MPa/km). In fact, the models with larger stress gradients produce only a small amount of deep afterslip, as the coseismic stress change is small compared to the preseismic stress. While these model
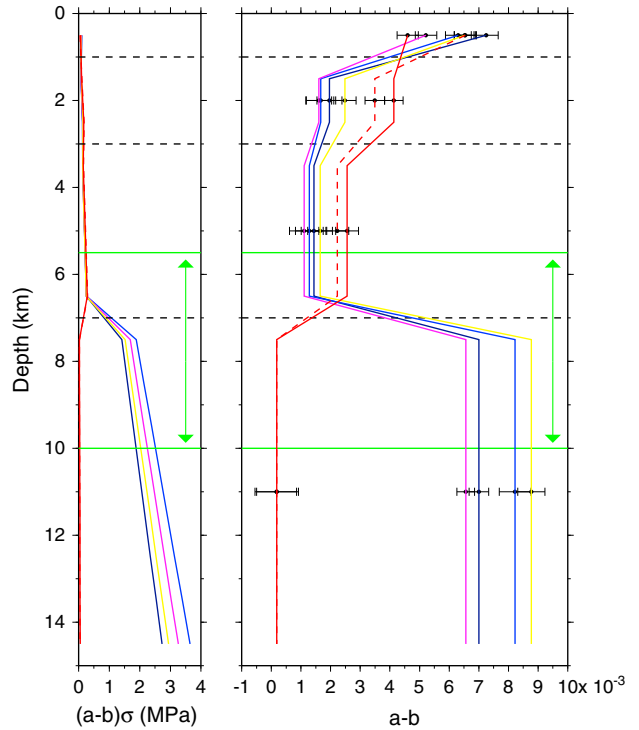
Figure 6. Depth variation of $(a$-$b)\sigma$ and a-b determined from the inversion of the GPS times series of postseismic displacements assuming coseismic slip Model B with different values of the stress gradient, $\frac{d(\sigma_1-\sigma_3)}{dz}$, of 5, 10, 20, 30, 40, and 50 MPa/km (dashed red, red, yellow, black, blue, and pink lines, respectively). The error bars show 2-σ standard deviation of a-b from the NA inversion. The horizontal black dashed lines denote the boundaries between the four layers. The horizontal green lines and arrows indicate the coseismic slip area of Model B, where presumably a negative value of a-b exists.

9

can fit the geodetic data reasonably well to first order, a previous joint analysis of coseismic and postseismic slip based on GPS and InSAR data has shown that substantial deep afterslip is actually needed to explain the observations [*Bruhat et al.*, 2011]. We therefore prefer the model obtained with a stress gradient of 10 MPa/km and coseismic slip Model B (Figures 2–4).This is also the model yielding the best RMS, though only marginally better than the model obtained with a stress gradient of 5 MPa/km.

[30] Our preferred model has a reference friction coefficient μ_* of 0.17, $a\text{-}b$ decreasing from 6.5×10^{-3} in layer 1 to 1.8×10^{-4} in layer 4, a vertical gradient of differential stress with depth of 10 MPa/km, and an assumed hydrostatic pore pressure ratio λ of 0.4. The model predicts afterslip in the area surrounding the coseismic rupture (Figure 2) as inferred from most kinematic inversions of GPS and InSAR data [*Johanson et al.*, 2006; *Bruhat et al.*, 2011].

[31] As shown in Figure 1, surface displacements cumulated over 548 days following the main shock are well matched by the model prediction, especially at the stations west of the fault trace. The model reproduces rapid postseismic velocities during the first 177 days as well as the less rapid velocities observed later on (Figure 3). The misfits are largest at the stations closest to the fault trace, probably because of the simplified fault geometry assumed in the model. The afterslip zone is observed to expand with time, surrounding the coseismic asperity and eventually penetrating into the coseismic zone.

[32] Figure 4 compares the slip measured at the surface at the location of the creepmeters with the slip predicted from our preferred model. While the fit to any single record is not great, the model yields a reasonable fit to these data overall. We observe that optimizing the fit at each single location would require changing the value of $a\text{-}b$ at the surface (i.e., in layer 1) by factors between 0.1 and 10 depending on the station. Two stations xta1 and xva1 near the central part along the fault trace need smaller $a\text{-}b$ to fit the creep data, and the other stations need larger values of $a\text{-}b$ instead. Altogether, these data suggest that there could be along strike variation of $a\text{-}b$ by about a factor 10 with respect to our reference model. We also notice that a few stations reveal significantly smaller cumulative afterslip, such as crr1 and xgh1, compared to those recorded at nearby stations suggesting that a fraction of the slip across the fault zone might take place on other subparallel fault strands.

6. Discussion

6.1. Comparison With Other Determinations of the Rate Parameter From Afterslip Studies

[33] We obtain a range of values of the rate parameter $a\text{-}b$ of 1.2 to 5.2×10^{-3} assuming uniform frictional properties but taking into account depth variation of effective normal stress. In our model, the average effective normal stress is 189 MPa, so $(a\text{-}b)\sigma$ ranges between 0.2 and 1.0 MPa. This is consistent with the analysis of *Barbot et al.* [2009] who estimated $a\text{-}b$ to be somewhat larger, about 7×10^{-3}, assuming a constant effective normal stress of 100 MPa (implying am average $(a\text{-}b)\sigma$ is 0.7 MPa). The values of $a\text{-}b$ obtained here are comparable to the values reported from afterslip

studies in various other tectonic contexts [e.g., *Hearn et al.*, 2002; *Miyazaki et al.*, 2004; *Perfettini and Avouac*, 2004, 2007; *Fukuda et al.*, 2009; *Hsu et al.*, 2006, 2009a, 2009b]. The values of $a\text{-}b$ at shallow depth are somewhat lower than the $6 - 13 \times 10^{-3}$ range derived by *Chang et al.* [2009] from the modeling of shallow seasonal creep and the afterslip of the 2003 M_w 6.8 Chengkung earthquake on the Chihshang fault (a high-angle reverse fault in eastern Taiwan).

[34] By contrast, our results differ from those obtained by *Johnson et al.* [2006] who estimated $a\text{-}b$ to be 10^{-4}–10^{-3} from dynamic modeling of the early postseismic period following the Parkfield earthquake based on a full rate-and-state dependent friction formulation (assuming an effective normal stress of 50 MPa). The reason for the discrepancy is not obvious. The two dynamic models should behave the same way past the initial transient increase of the sliding velocity from $V_0 \exp\left(\frac{\Delta\tau}{a\sigma}\right)$ to $V_0\exp\left(\frac{\Delta\tau}{(a-b)\sigma}\right)$, because the transient phase is actually not observed. Even in the subdaily GPS data, the rate-and-state model allows large trade-off between the values of $a\text{-}b$ and d_c. We think that this trade-off might explain the discrepancy between the two studies.

6.2. Preseismic Stress and Reference Friction

[35] Due to strong trade-offs among the model parameters, the preseismic stress level acting on the fault and its reference friction coefficient cannot be constrained really tightly. One way to limit that trade-off is to resort to independent a priori constraints. *Fialko et al.* [2005] analyzed the influence of topography on the tectonic stress field as revealed by focal mechanisms of earthquakes. They deduced that the average differential stress in the upper crust around the San Andreas Fault is probably of the order of 50 MPa in the 0–15 km seismogenic depth range. This would imply a stress gradient $\frac{d(\sigma_1-\sigma_3)}{dz}$ of the order of 10 MPa/km, which indeed agrees with our preferred model. This would then imply a reference friction coefficient μ_* between 0.1 and 0.17. Note that our model is sensitive only to the effective friction $\mu(1 - \lambda)$ so that it could be argued that the apparent low friction could be due to high pore pressure. Because of the in situ observation of hydrostatic pore pressure in the SAFOD drill hole, we favor the hypothesis of an intrinsically low friction.

6.3. Comparison With Laboratory Measurements of Fault Friction Properties

[36] Our estimates of $a\text{-}b$ compare generally well with the typical 0 to 6×10^{-3} range of values obtained from laboratory experiments, but the 0.1–0.17 reference friction is at the lower end of experimental values [e.g., *Marone*, 1998]. Our results can also be compared with frictional properties measured directly on samples from the San Andreas Fault Observatory at Depth (SAFOD) project. This comparison should be considered with caution as those samples do not necessarily represent the properties of the Parkfield fault segment. SAFOD was indeed drilled at its northern junction with the creeping segment of the San Andreas Fault where the fault cuts through the Coast Range Ophiolite [*Irwin and Barnes*, 1975; *Moore and Rymer*, 2012].

[37] Samples collected at a depth of 2.7 km have been shown to obey dominantly a rate-strengthening friction law with $a\text{-}b$ values of 4 to 20×10^{-3} for samples collected outside the

Table 3. Different Slip Thresholds of Relocking of Coseismic Rupture

No Afterslip Area	Coseismic Slip $\geq$ 0.1 m	Coseismic Slip $\geq$ 0.2 m	Coseismic Slip $\geq$ 0.3 m	Coseismic Slip $\geq$ 0.4 m
RMS (mm)	15.15	6.09	5.77	5.88
V_0 (mm/yr)[a]	20.0	23.0	24.5	25.4
M_0 ($\times 10^{18}$ N m)[b]	1.6	2.1	2.2	2.3
M_w[b]	6.1	6.18	6.2	6.2

[a]The value of V_0 is an average result on the fault plane calculated from equation (12).
[b]M_0 and M_w are accumulated values up to 548 days after the main shock.

foliated gouge and somewhat lower values of about 1 to 10×10^{-3} for samples within strongly deformed zones [*Lockner et al.*, 2011; *Carpenter et al.*, 2012]. This is remarkably consistent with the values obtained in our analysis from assuming either uniform or depth-varying frictional rate dependency.

[38] The range of reference friction values between 0.1 and 0.5 in our models is also consistent with the range of values reported from experimental measurements on samples from the SAFOD borehole [*Carpenter et al.*, 2009, 2011, 2012] and from cuttings and spot core samples retrieved during SAFOD phases 1 and 2 [*Tembe et al.*, 2006]. Our preferred model, which corresponds to a rather low gradient of differential stress (10 MPa/km), implies a reference friction at the lower end of this spectrum, between 0.1 and 0.17, which is comparable to the friction of 0.15 to 0.19 measured directly on fault gouges of the SAFOD core [*Lockner et al.*, 2011; *Carpenter et al.*, 2011, 2012]. It should be kept in mind that our estimates represent spatial averages of heterogeneous properties. Note however that the averaging is done only within those areas that produce afterslip (areas that are rate weakening are not probed in our analysis).

[39] The consistency of our results with laboratory measurements of rock frictional properties should be considered with caution as most of the laboratory values were obtained at room temperature and under dry conditions. How the properties measured in laboratory studies can be scaled up to apply to natural faults with heterogeneous properties is another caveat. Also, there is a possibility that postseismic slip could be due to strain distributed within a fault zone with finite width.

6.4. Variability of Friction Rate Parameters

[40] While a satisfactory fit to the geodetic data is obtained assuming uniform fault friction properties, there is no doubt that friction properties must vary spatially quite substantially. Spatial heterogeneities of friction must be present to account for the variability of the postseismic signal recorded by the creepmeters and more generally the spatial proximity of patches producing afterslip ($a\text{-}b > 0$) or nucleating seismic slip during the main shock or aftershocks ($a\text{-}b < 0$). Some general trend in the mean value of the rate parameter can nonetheless be recognized. The main reason that the four-layer models fit the data better is that it allows larger values of $a\text{-}b$ at shallow depth compared to the value in the 1–5 km depth range. So we believe that this trend is a correct and robust inference. The general increase of $a\text{-}b$ values toward the surface inferred in this study is consistent with the view that the lesser consolidation of fault gouge at lower pressure should enhance the rate-strengthening effect. This

effect is observed in experiments on unconsolidated gouge at varying normal stress which show that $a\text{-}b$ increases from ~1 to ~5×10^{-3} when normal stress decreases from 170 to 50 MPa [*Marone*, 1998]. These values are qualitatively consistent with our results which show an increase of $a\text{-}b$ from $1\text{--}2 \times 10^{-3}$ in the 3–7 km depth range to 4–
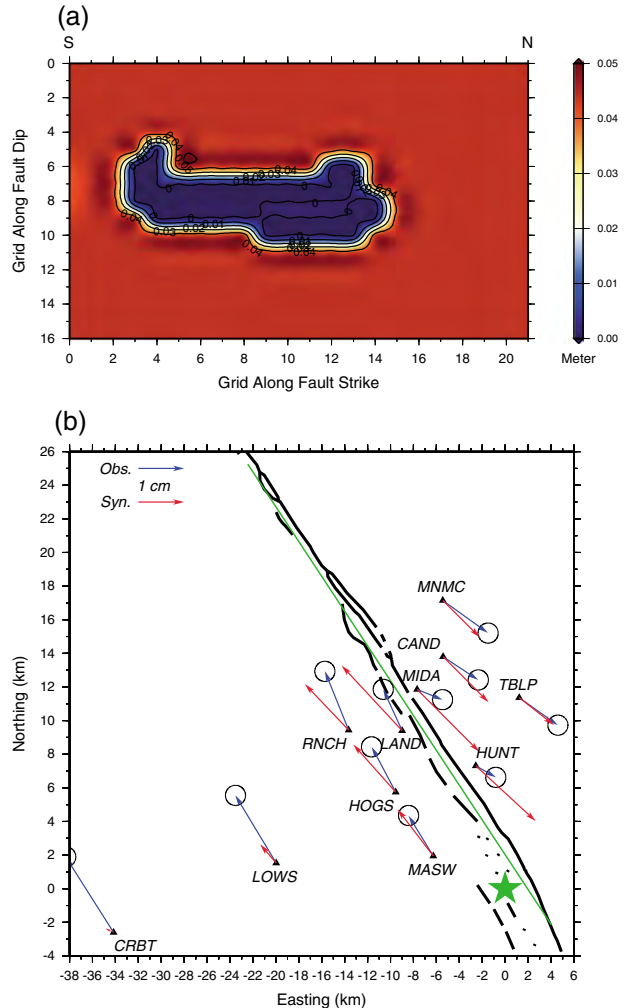
Figure 7. (a) Interseismic fault creep predicted after 548 days from the dynamic model derived from the inversion of the postseismic data assuming a vertical gradient of differential stress of 10 MPa/km and the 2004 Parkfield coseismic slip Model B. Relocking is imposed where the 2004 coseismic slip exceeds 0.3 m. (b) Comparison of predicted and measured interseismic velocities at 11 GPS stations.
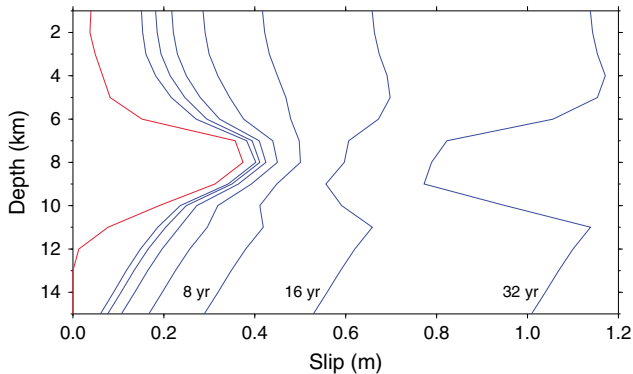
Figure 8. Model-predicted long-term cumulative displacements following the 2004 earthquake as a function of depth. The red line represents the average coseismic slip, and the blue lines are the average slip at different times after the Parkfield earthquake. The long-term cumulative displacements are computed by our dynamic afterslip model with our preferred model case, that is, coseismic slip Model B in input and depth variations of a-b and assuming a vertical gradient of differential stress of 10 MPa/km. Interseismic creep is taken into account.

7×10^{-3} at 0–1 km depth (when we consider only the results obtained with coseismic slip Model B as input). This would also be consistent with the larger values of 13×10^{-3} at 0–100 m shallow depth and of $6 - 7 \times 10^{-3}$ in the 0.1–5 km depth range estimated for the Chihshang fault [*Chang et al.*, 2009].

6.5. Effect of Relocking of Rate-Weakening Fault Patches

[41] We have put the emphasis so far on discussing the frictional properties of the regions that are rate strengthening and contribute to afterslip. In fact, the seismic activity requires that rate-weakening patches must also exist although they were ignored in our modeling. We have indeed assumed that the whole fault, including the coseismic area, obeys a rate-strengthening friction law. This is a difference with the dynamic models of *Barbot et al.* [2009] and Johnson *et al.* [2006], who imposed relocking of the ruptured area. The models presented above thus allow aseismic creep to propagate into the area that was ruptured coseismically. As a matter of fact, these models all yield distributions of cumulated afterslip at the end of the period which partly overlaps with the coseismic rupture. After a longer period than considered in this study, the whole fault would end up creeping at a constant slip rate preventing any renewed rupture. This is unphysical. There must be in reality rate-weakening areas that relock in the postseismic period, in particular within the area that ruptured in 2004 so that the earthquake could nucleate there. These areas should not creep in the postseismic period. In order to assess that possibility and assess the effect of relocking, we ran a set of inversions assuming complete relocking (as would happen with a rate-weakening law) of a variable fraction of the coseismic area. That fraction is varied by assuming that relocking occurs where coseismic slip exceeds some variable threshold value. The

settings of these inversions are otherwise the same as the one corresponding to the preferred model described in the previous section: four layers, a stress gradient of 10 MPa/km, and with coseismic slip Model B as an initial input model. Results are listed in Table 3. Isocontours of coseismic slip, which determined the relocked areas in those models, are shown in Figure 2a. When the threshold is set to 0.3 m or higher, the fit to the data is very good with an RMS about equal to the value of 5.77 mm RMS obtained with the initial model. In these cases, relocking of a fraction of the seismic rupture area does not improve the fit to the data (Table 3). If we force relocking of a larger fraction of the rupture area, then the RMS increases significantly. It is clear that the coseismic slip area is not totally locked after the main shock and that some afterslip must be allowed where coseismic slip was lower than about 0.3 m. So it seems that the relocked area, presumably obeying rate-weakening friction, is somewhat smaller than the rupture area of Model B. This could be taken as an indication that the rupture propagated in the rate-strengthening domain, as is observed in dynamic models of seismic ruptures. Our observation does not necessarily point to a strong dynamic weakening effect [*Noda and Lapusta*, 2013] and would be consistent with dyanic simulations results based on regular rate-and-state friction [*Barbot et al.*, 2012].

[42] Assuming relocking where coseismic slip exceeded 0.3 m is a good compromise as it also satisfies the condition that some deficit of slip must accumulate in the interseismic period within the rupture area of the 2004 earthquake, as models of interseismic strain have shown [*Murray and Langbein*, 2006; *Barbot et al.*, 2012]. Stress shadow effects are not taken into account in our model, and this would improve the fit to the data of the nearby field stations [*Bürgmann et al.*, 2005; *Hetland and Simons*, 2010]. Figure 7 shows the prediction of our dynamic model, with relocking of the coseismic area where coseismic slip is larger than 0.3 m, after full relaxation of coseismic stresses (computed from equation (12)). The model predicts interseismic displacements in quite good agreement with those measured during the interseismic period that preceded the 2004 earthquake. The fit to the distant stations is not very good, however, as this model ignores the influence of other sources of deformation than creep on our fault model (e.g., creep at greater depth and on adjacent fault segments). Figure 8 next shows the time evolution of average slip (average over depth bins) as a function of time predicted from this dynamic model starting with the imposed coseismic model. Steady creep and transient aseismic slip around the coseismic slip patches smooth out the effect of the coseismic rupture in about 16 years. This is thus the time needed to reload the coseismic area to produce a new rupture with a slip potency (integral of slip over rupture area) similar to that of the 2004 earthquake. This recurrence time is close the ~20 years average return period of M_w 6.0 earthquakes on that segment over the last century and half [*Bakun et al.*, 2005].

[43] The afterslip model would be about the same if we had assumed two parallel planes (one being rate strengthening and the other rate weakening). However, in that case, there would be no reason for relocking of the rupture area and interseismic buildup would not happen. So it makes more sense to assume that we have only one plane in the model.

7. Conclusions

[44] This study demonstrates that the GPS measurements of postseismic displacements following the Parkfield earthquake of 2004 can be reproduced from a simple dynamic model of afterslip which assumes a quite simple logarithmic rate-strengthening friction law and depends on a small number of free parameters (6 in the most complex models shown above). The quality of the fit is comparable to that obtained from kinematic inversions which involve an order of magnitude larger number of free parameters and require nonphysical regularization constraints. In dynamic modeling of afterslip, the space of possible solutions is quite restricted given the limit number of model parameters. It is remarkable that the same dynamic models obtained from these inversions fit the preseismic and postseismic data reasonably well. This suggests that the basic laws entering the dynamic model are probably correct, the key ingredients being that the friction law is rate strengthening and that friction varies as the logarithm of the sliding velocity.

[45] The modeling approach presented in this study is more general than the approach adopted in previous studies in that it takes the prestress explicitly into account and therefore allows discussing the consistency between the preseismic stress, the slip rate distribution before the main shock, and the friction law. This allows for tighter constraints on the estimated friction properties. Strong trade-offs among the model parameters do, however, require independent constraints. If the stress level can be constrained, and adopting the relatively low deviatoric values proposed by *Fialko et al.* [2005], we find that the reference friction (the friction at a sliding rate of 30 mm/yr) is quite low in the order of 0.1–0.2 assuming a hydrostatic pore pressure. This result is consistent with experimental measurements on core samples [*Lockner et al.*, 2011; *Carpenter et al.*, 2011, 2012] and favors the view that the friction on the creeping patches of the San Andreas Fault would be intrinsically low due to its mineralogy and mineral fabric. We report values of *a-b*, the friction rate parameter characterizing the rate-strengthening dependency of friction, similar to experimental values and find that the rate strengthening is enhanced at shallower depth. Relocking occurred within only a small fraction of the coseismic rupture model suggesting that the seismic rupture was able to propagate into rate-strengthening regions. Spatial heterogeneities of frictional properties must be present to account for some key observations (e.g., the variability of the creepmeter data, the coexistence of small earthquakes, and afterslip on a given fault patch) but are not analyzed here. Taking these heterogeneities into account in dynamic modeling is a challenge that needs to be addressed in future studies.

Appendix A: Results Obtained With Coseismic Model A

[46] We describe here the results obtained using coseismic slip Model A as an input in the dynamic modeling of afterslip. Different cases carried out with Model A also consider four layers with different *a-b* values embedded in an elastic half-space. The coseismic rupture Model A was derived by
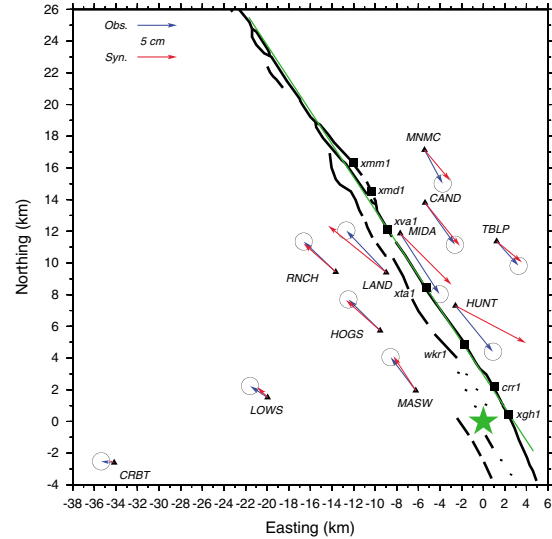

Figure A1. Observed and predicted postseismic displacements due to the M_w 6.0 earthquake of 2004 on the Parkfield segment of the San Andreas Fault. Blue arrows with 2-σ uncertainties ellipses show cumulative postseismic displacements up to 548 days after the main shock derived from the SOPAC GPS time series. Red arrows show corresponding predicted displacements for the four layer velocity-strengthening model with the coseismic source Model A. Black line shows fault trace, and green line shows the location of the vertical planar fault model assumed in this study. Green star shows the epicenter of the 2004 Parkfield earthquake, and black squares show locations of creepmeters.

Bruhat et al. [2011] based on geodetic and InSAR data and is depicted in Figure A1.

[47] From Table 2, we can see that the values of RMS for different cases of Model A are very similar to each other. We arbitrarily select the case with $d(\sigma_1 - \sigma_3)/dz = 30$ MPa/km of Model A to describe the results here. Figure A1 shows the fit to postseismic surface displacements accumulated up to 548 days after the main shock at the 11 continuous GPS stations. Except at the HUNT station, the fitness is very similar to the results of Model B. Temporal variation of the afterslip shows that the afterslip occurred at the top of the major coseismic asperity initially and progressed downdip to the depth from the gap between the two coseismic asperities (Figure A2). The region of afterslip expanded with time and finally surrounded the coseismic asperities. The afterslip did occur within the asperities at locations with coseismic slip less than 0.2 m, and the afterslip at shallow depth is greater than that at deeper parts of the fault plane. This model can also fit the GPS time series of postseismic displacements well during a 548 days period following the earthquake except for the sites close to the fault trace (Figure A3). We observe that the model reproduces rapid postseismic velocities during the first 75 days and less rapid velocities during the later time periods. The average root-mean-square of this model is 6.94 mm which is slightly higher than that of the other model (Model B) using
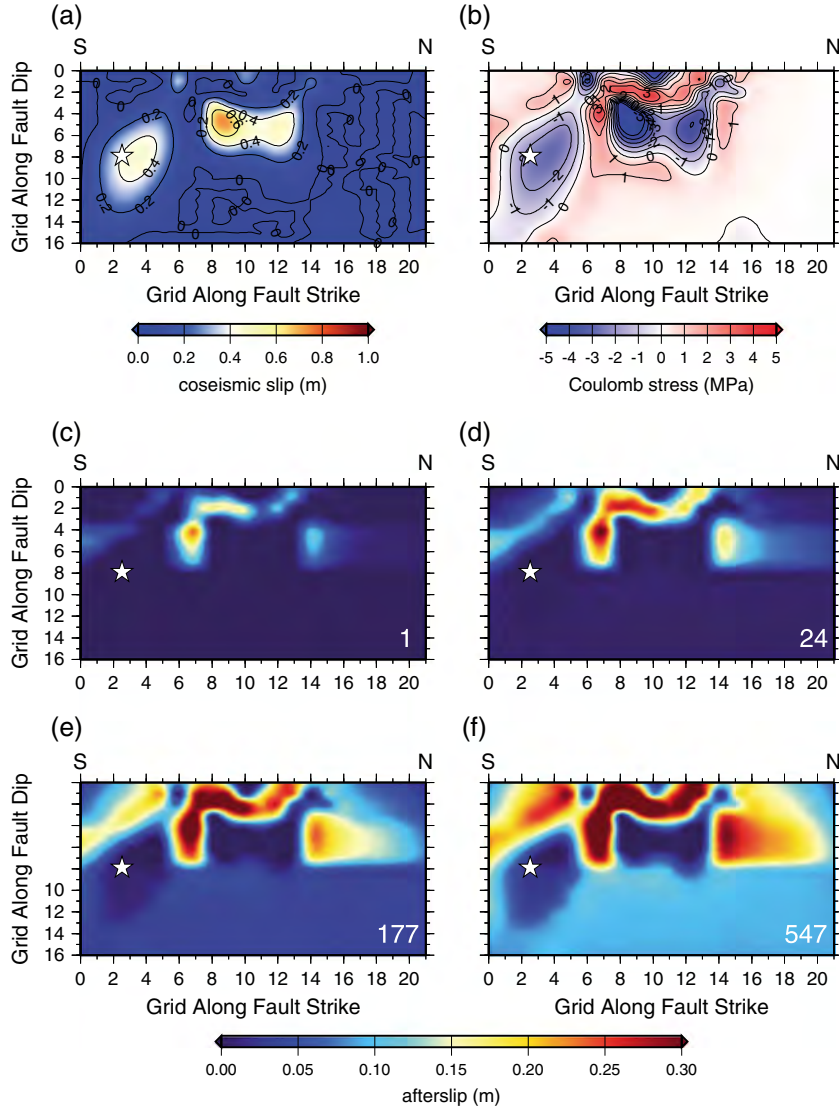
Figure A2. (a) Coseismic slip distribution and (b) the coseismic Coulomb failure stress changes on the fault plane corresponding to coseismic Model A, and (c–f) predicted postseismic slip over different time periods. The coseismic slip distribution shown in Figure A2a was determined from the inversion of GPS and InSAR data [*Bruhat et al.*, 2011]. Temporal variation of the afterslip predicted from dynamic modeling (Figures A2c–A2f) in a case which yielded a static friction μ_s= 0.37, a depth variable rate dependency of friction (considering four layers with a-b values represented in Figures A4), and a vertical gradient of differential stress $\frac{d(\sigma_1 - \sigma_3)}{dz}$ = 30 MPa/km. White numbers in Figures A2c–A2f show number of days after the main shock (28 September 2004). The white star indicates the focus of the main shock.

the coseismic rupture and fault geometry of Barbot *et al.* (2012). The values of inverted reference friction coefficients and the trend of depth-dependent *a-b* are similar to that of Model B. As shown in Figure A4, the values of *a-b* decreased with depth from 20×10^{-3} near the surface down to 1.2×10^{-3} at depths with larger coseismic slip and then increased up to $10–16 \times 10^{-3}$ at deeper parts of the fault plane with smaller coseismic slip. On the other hand, the resulting interseismic creeping rate of 80.8 mm/yr is much higher than the one derived from both Model B and geodetic/geological data.

Appendix B: Comparison of 2-D Dynamic Models of Afterslip With Theoretical Predictions From a Spring-and-Slider Model

[48] It is common practice to derive frictional parameters through comparison of postseismic displacements, or inverted afterslip with the prediction of a 1-D spring-and-slider model [e.g., *Hsu et al.*, 2006; *Perfettini et al.*, 2010]. This approach ignores the fact that the afterslip zone spreads with time. Frictional properties derived based on the 1-D approximation might therefore be biased. To
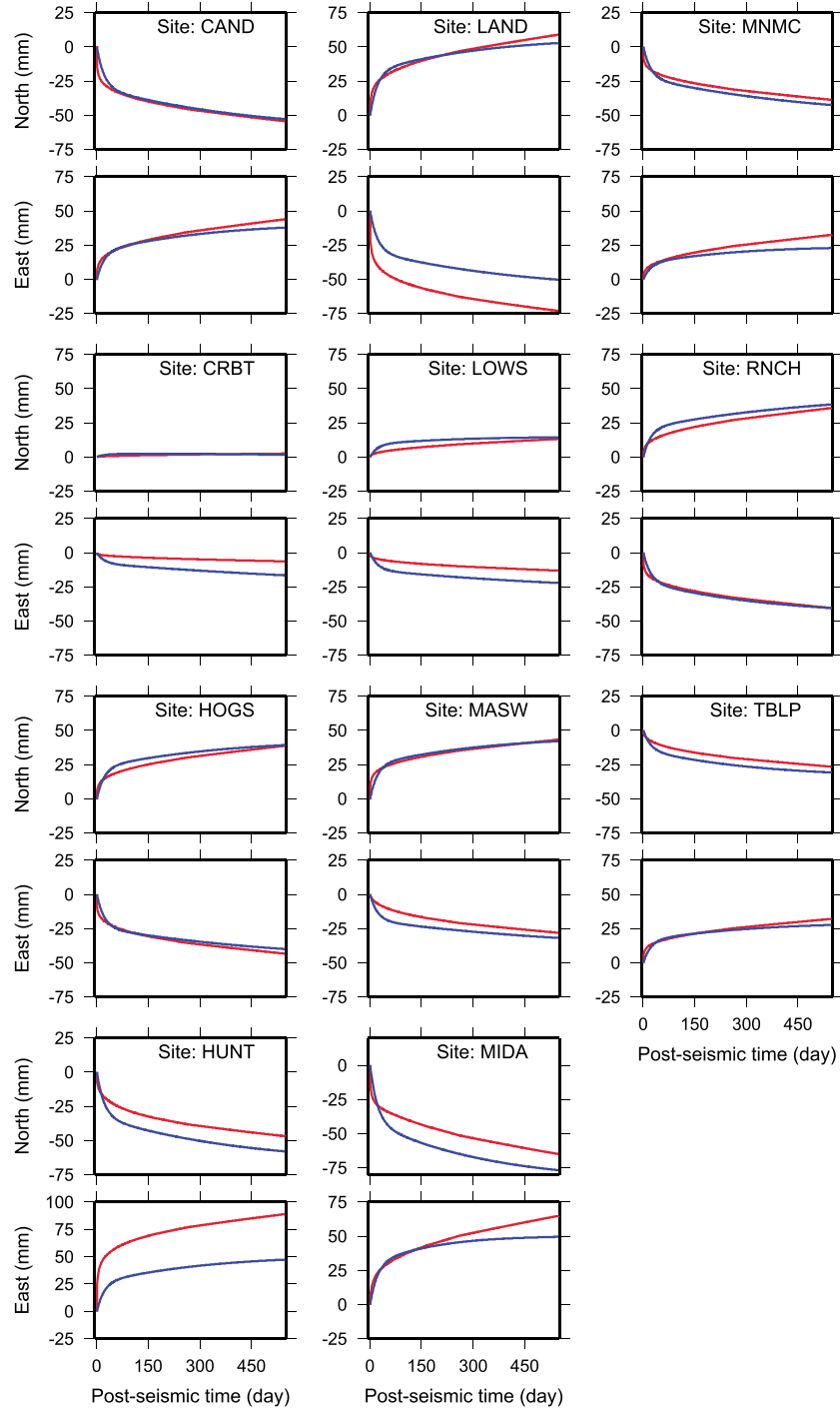
Figure A3. The comparisons between the modeled and observed values of the postseismic continuous GPS time series at all 11 stations in a case with coseismic source Model A. The Blue line is the observed GPS time series, and the red line is the modeled time series generated by the layer Model A with $\frac{d(\sigma_1-\sigma_3)}{dz} = 30$ MPa/km.

evaluate that possibility, we used the prediction of our dynamic model of slip at two points on the fault (at depths of 4.5 and 11.5 km, respectively, updip and downdip of the rupture area) and determined the value of *a-b* required to reproduce these slip histories with a 1-D model. We used the
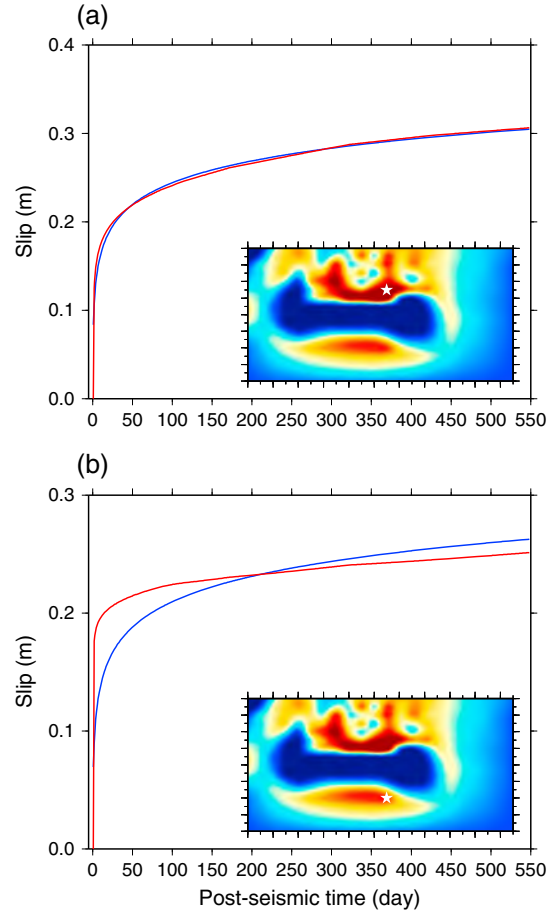
formulation of *Perfettini and Avouac* [2004], assuming a long-term slip rate $V_{pl} = V_* = 30$ mm/yr. The 1-D model fits quite accurately the time evolution of slip at the shallower point but does not fit very well at the deeper point (Figure B1). The 1-D spring and slider approach requires a
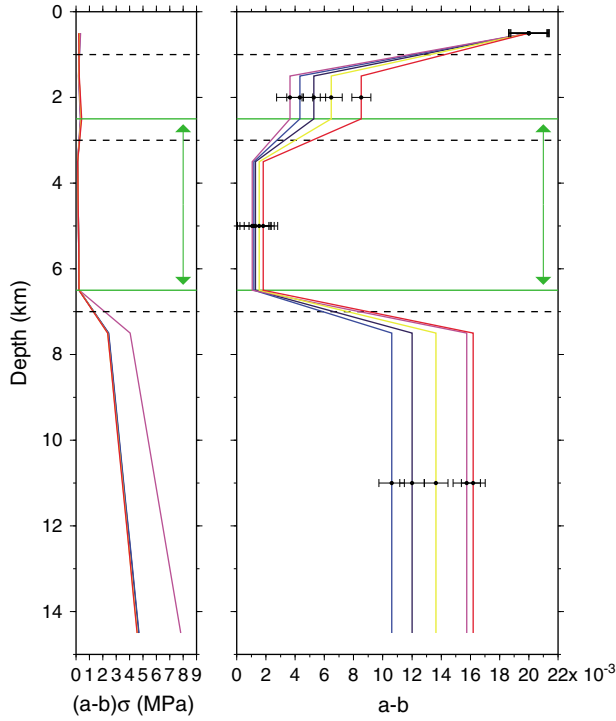
Figure A4. Depth variation of $(a\text{-}b)\sigma$ and $a\text{-}b$ determined from the inversion of the GPS times series of postseismic displacements with coseismic source Model A and different values of $\frac{d(\sigma_1-\sigma_3)}{dz}$ of 10, 20, 30, 40, and 50 MPa/km (red, yellow, black, blue, and pink lines, respectively). The error bars show 2-σ standard deviation of $a\text{-}b$ from the NA inversion. The horizontal black dashed lines denote the boundaries between the four layers. The horizontal green lines and arrows indicate the coseismic slip area of the Model A, presumably of a negative value of $a\text{-}b$.

Figure B1. Comparisons of 1-D spring and slider modeling (red curves) with our preferred dynamic model (blue curves) for two points (white stars) at (a) 4.5 km and (b) 11.5 km depth. Our preferred model: four layers, coseismic Model B, and $d(\sigma_1-\sigma_3)/dz = 10$ MPa/km. The 1-D spring and slider model: $U(t) \approx V_{pl}t_r \log[1+(V^+/V_{pl}t_r)t]$ [*Perfettini and Avouac*, 2004].

value of relaxation time $t_r = 1.19$ year and $\frac{V_+}{V_{pl}} = 4085$ to fit the higher afterslip rate on the fault patch at depth 4.5 km and inferred a value of $a\text{-}b = 2.4 \times 10^{-3}$ from the equation $\Delta CFF = (a\text{-}b)\sigma\log(V_+/V_{pl})$. Similarly, we estimate $t_r = 1.04$ year and $\frac{V_+}{V_{pl}} = 3139$ to fit the afterslip on the patch at 11.5 km depth. We then get $a\text{-}b = 1.2 \times 10^{-3}$. These two values are of the same order as our inverted $a\text{-}b$, especially at the shallower fault patch, showing that although the 2-D might be a cause for discrepancies between the 1-D predicted and actual fault slip, estimates of $a\text{-}b$ derived from the 1-D approximation are not significantly biased.

References

Allmann, B. P., and P. M. Shearer (2007), A high-frequency secondary event during the 2004 Parkfield earthquake, *Science*, *318*, 1279–1283.

Bakun, W., and T. McEvilly (1984), Recurrence models and Parkfield, California, earthquake, *J. Geophys. Res.*, *89*, 3051–3058, doi:10.1029/JB089iB05p03051.

Bakun, W. H., et al. (2005), Implications for prediction and hazard assessment from the 2004 Parkfield earthquake, *Nature*, *437*, 969–974, doi:10.1038/nature04067.

Barbot, S., Y. Fialko, and Y. Bock (2009), Postseismic deformation due to the Mw 6.0 2004 Parkfield earthquake: Stress-driven creep on a fault with spatially variable rate-and-state friction parameters, *J. Geophys. Res.*, *114*, B07405, doi:10.1029/2008JB005748.

Barbot, S., N. Lapusta, and J.-P. Avouac (2012), Under the hood of the earthquake machine: Toward predictive modeling of the seismic cycle, *Science*, *336*, 707–710, doi:10.1126/science.1218796.

Bennington, N., C. Thurber, K. L. Feigl, and J. Murray-Moraleda (2011), Aftershock distribution as a constraint on the geodetic model of coseismic slip for the 2004 Parkfield earthquake, *Pure Appl. Geophys.*, *168*, 1553–1565.

Bruhat, L., S. Barbot, and J.-P. Avouac (2011), Evidence for postseismic deformation of the lower crust following the 2004 Mw 6.0 Parkfield earthquake, *J. Geophys. Res.*, *116*, B08401, doi:10.1029/2010JB008073.

Brune, J. N., T. Henyey, and R. Roy (1969), Heat flow, stress, and rate of slip along San Andreas Fault, California, *J. Geophys. Res.*, *74*, 3821–3827, doi:10.1029/JB074i015p03821.

Bürgmann, R., M. G. Kogan, G. M. Steblov, G. Hilley, V. E. Levin, and E. Apel (2005), Interseismic coupling and asperity distribution along the Kamchatka subduction zone, *J. Geophys. Res.*, *110*, B07405, doi:10.1029/2005JB003648.

Byerlee, J. D. (1978), Friction of rock, *Pure Appl. Geophys.*, *116*, 615–626.

Carpenter, B. M., C. Marone, and D. M. Saffer (2009), Frictional behavior of materials in the 3D SAFOD volume, *Geophys. Res. Lett.*, *36*, L05302, doi:10.1029/2008GL036660.

Carpenter, B. M., C. Marone, and D. M. Saffer (2011), Weakness of the San Andreas Fault revealed by samples from the active fault zone, *Nat. Geosci.*, *4*, 251–254, doi:10.1038/ngeo1089.

Carpenter, B. M., D. M. Saffer, and C. Marone (2012), Frictional properties and sliding stability of the San Andreas Fault from deep drill core, *Geology*, *40*(8), 759–762, doi:10.1130/G33007.

Chang, S.-H., W.-H. Wang, and J.-C. Lee (2009), Modeling surface creep of the Chihshang fault in eastern Taiwan with velocity-strengthening friction, *Geophys. J. Int.*, *176*(2), 601–613, doi:10.0000/j.1365-246X.2008.03995.x.

Dieterich, J. H. (1979), Modeling of rock friction: 1. Experimental results and constitutive equations, *J. Geophys. Res.*, *84*, 2161–2168.

Fialko, Y., L. Rivera, and H. Kanamori (2005), Estimate of differential stress in the upper crust from variations in topography and strike along the San Andreas Fault, *Geophys. J. Int.*, *160*, 527–532, doi:10.1111/j.1365-246X.2004.02511.x.

Freed, A. M. (2007), Afterslip (and only afterslip) following the 2004 Parkfield, California, earthquake, *Geophys. Res. Lett.*, *34*, L06312, doi:10.1029/2006GL029155.

Fukuda, J., K. M. Johnson, K. Larson, and S. Miyazaki (2009), Fault friction parameters inferred from the early stages of afterslip following the 2003 Tokachi-oki earthquake, *J. Geophys. Res.*, *114*, B04412, doi:10.1029/208JB006166.

Hardebeck, J. L., and E. Hauksson (2001), Crustal stress field in southern California and its implications for fault mechanics, *J. Geophys. Res.*, *106*(B10), 21,859–21,882.

Hearn, E., R. Burgmann, and R. Reilinger (2002), Dynamics of Izmit earthquake postseismic deformation and loading of the Duzce earthquake hypocenter, *Bull. Seismol. Soc. Am.*, *92*, 172–193.

Hetland, E. A., and M. Simons (2010), Post-seismic and interseismic fault creep. II: Transient creep and interseismic stress shadows on megathrusts, *Geophys. J. Int.*, *181*, 99–112.

Hickman, S., and M. D. Zoback (2004), Stress orientations and magnitudes in the SAFOD pilot hole, *Geophys. Res. Lett.*, *31*, L15S12, doi:10.1029/2004GL020043.

Hickman, S., M. D. Zoback, and W. L. Ellsworth (2004), Introduction to special section: Preparing for the San Andreas Fault Observatory at Depth, *Geophys. Res. Lett.*, *31*, L12S01, doi:10.1029/2004GL020688.

Hsu, Y.-J., M. Simons, J.-P. Avouac, J. Galetzka, K. Sieh, M. Chlieh, D. Natawidjaja, L. Prawirodirdjo, and Y. Bock (2006), Frictional afterslip following the Mw 8.7, 2005 Nias-Simeulue earthquake, Sumatra, *Science*, *312*, 1921–1926.

Hsu, Y.-J., S.-B. Yu, and H.-Y. Chen (2009a), Coseismic and postseismic deformation associated with the 2003 Chengkung, Taiwan, earthquake, *Geophys. J. Int.*, *176*(2), 420–430.

Hsu, Y.-J., J.-P. Avouac, S.-B. Yu, C.-H. Chang, Y.-M. Wu, and J. Woessner (2009b), Spatio-temporal slip, and stress level on the faults within the western foothills of Taiwan: Implications for fault frictional properties, *Pure Appl. Geophys.*, *166*(10–11), 1853–1884.

Irwin, W. P., and I. Barnes (1975), Effect of geologic structure and metamorphic fluids on seismic behavior of the San Andreas Fault system in central and northern California, *Geology*, *3*(12), 713–716.

Johanson, I. A., E. J. Fielding, F. Rolandone, and R. Bürgmann (2006), Coseismic and postseismic slip of the 2004 Parkfield earthquake from space-geodetic data, *Bull. Seismol. Soc. Am.*, *96*, S269–S282, doi:10.1785/0120050818.

Johnson, K. M., R. Bürgmann, and K. Larson (2006), Frictional properties on the San Andreas Fault near Parkfield, California, inferred from models of afterslip following the 2004 earthquake, *Bull. Seismol. Soc. Am.*, *96*, S321–S338, doi:10.1785/0120050808.

Lachenbuch, A. H., and J. H. Sass (1980), Heat flow and energetics of the San Andreas Fault zone, *J. Geophys. Res.*, *85*, 6185–6223.

Langbein, J., and Y. Bock (2004), High rate real time GPS network at Parkfield: Utility for detecting fault slip and seismic displacements, *Geophys. Res. Lett.*, *31*, L15S20, doi:10.1029/2003GL019408.

Langbein, J., J. R. Murray, and H. A. Snyder (2006), Coseismic and initial postseismic deformation from the 2004 Parkfield, California, earthquake, observed by Global Positioning System, electronic distance meter, creepmeter, and borehole strainmeters, *Bull. Seismol. Soc. Am.*, *96*, S304–S320, doi:10.1785/0120050823.

Lengliné, O., and D. Marsan (2009), Inferring the coseismic and postseismic stress changes caused by the 2004 Mw = 6 Parkfield earthquake from variations of recurrence times of microearthquakes, *J. Geophys. Res.*, *114*, B10303, doi:10.1029/2008JB006118.

Linker, M. F., and J. R. Rice (1997), Models of postseismic deformation and stress transfer associated with the Loma Prieta earthquake, in The Loma

Prieta Earthquake of October 17, 1989, *U.S. Geol. Surv. Prof. Pap.*, *1550-D*, 253–275.

Lisowski, M., J. Savage, and W. H. Prescott (1991), The velocity field along the San Andreas Fault in central and southern California, *J. Geophys. Res.*, *96*, 8369–8389, doi:10.1029/91JB00199.

Lockner, D. A., C. Morrow, D. Moore, and S. Hickman (2011), Low strength of deep San Andreas Fault gouge from SAFOD core, *Nature*, *472*, 82–85, doi:10.1038/nature09927.

Marone, C. (1998), Laboratory-derived friction laws and their application to seismic faulting, *Annu. Rev. Earth Planet. Sci.*, *26*, 643–696.

Marone, C., C. H. Scholz, and R. Bilham (1991), On the mechanisms of earthquake afterslip, *J. Geophys. Res.*, *96*, 8441–8452.

Miyazaki, S., P. Segall, J. Fukuda, and T. Kato (2004), Space time distribution of afterslip following the 2003 Tokachi-oki earthquake: Implications for variations in fault zone frictional properties, *Geophys. Res. Lett.*, *31*, L06623, doi:10.1029/2003GL019410.

Moore, D. E., and M. J. Rymer (2012), Correlation of clayey gouge in a surface exposure of serpentinite in the San Andreas Fault with gouge from the San Andreas Fault Observatory at Depth (SAFOD), *J. Struct. Geol.*, *38*, 51–60.

Mount, V. S., and J. Suppe (1987), State of stress near the San Andreas Fault: Implications for wrench tectonics, *Geology*, *15*, 1143–1146.

Murray, J., and J. Langbein (2006), Slip on the San Andreas Fault at Parkfield, California, over two earthquake cycles, and the implications for seismic hazard, *Bull. Seismol. Soc. Am.*, *96*, S283–S303, doi:10.1785/0120050820.

Murray, J. R., P. Segall, P. Cervelli, W. Prescott, and J. Svarc (2001), Inversion of GPS data for spatially variable slip-rate on the San Andreas Fault near Parkfield, CA, *Geophys. Res. Lett.*, *28*, 359–362.

Niemeijer, A. R., and C. J. Spiers (2006), Velocity dependence of strength and healing behaviour in simulated phyllosilicate-bearing fault gouge, *Tectonophysics*, *427*, 231–253.

Noda, H., and N. Lapusta (2013), Stable creeping fault segments can become destructive as a result of dynamic weakening, *Nature*, *493*, 518–521, doi:10.1038/nature11703.

Okada, Y. (1992), Internal deformation due to shear and tensile faults in a half-space, *Bull. Seismol. Soc. Am.*, *82*, 1018–1040.

Perfettini, H., and J.-P. Ampuero (2008), Dynamics of a velocity strengthening region: Implications for slow earthquakes and postseismic slip, *J. Geophys. Res.*, *113*, B09411, doi:10.1029/2007JB005398.

Perfettini, H., and J.-P. Avouac (2004), Postseismic relaxation driven by brittle creep: A possible mechanism to reconcile geodetic measurements and the decay rate of aftershocks, application to the Chi-Chi earthquake, Taiwan, *J. Geophys. Res.*, *109*, B02304, doi:10.1029/2003JB002488.

Perfettini, H., and J.-P. Avouac (2007), Modeling afterslip and aftershocks following the 1992 Landers earthquake, *J. Geophys. Res.*, *112*, B07409, doi:10.1029/2006JB004399.

Perfettini, H., et al. (2010), Seismic and aseismic slip on the central Peru megathrust, *Nature*, *465*, 78–81, doi:10.1038/nature09062.

Provost, A. S., and H. Houston (2001), Orientation of the stress field surrounding the creeping section of the San Andreas Fault: Evidence for a narrow mechanically weak fault zone, *J. Geophys. Res.*, *106*(B6), 11,373–11,386.

Ruina, A. L. (1983), Slip instability and state variable friction laws, *J. Geophys. Res.*, *88*, 10,359–10,370.

Sambridge, M. (1999), Geophysical inversion with a neighbourhood algorithm—I. Searching a parameter space, *Geophys. J. Int.*, *138*, 479–494.

Scholz, C. H. (2000), Evidence for a strong San Andreas Fault, *Geology*, *28*, 163–166.

Scholz, C. H. (2002), *The Mechanics of Earthquakes and Faulting*, 2nd ed. 471 pp., Cambridge Univ. Press, New York.

Stuart, W. D., and T. E. Tullis (1995), Fault model for preseismic deformation at Parkfield, California, *J. Geophys. Res.*, *100*, 24,079–24,099, doi:10.1029/95JB02517.

Tembe, S., D. A. Lockner, J. G. Solum, C. A. Morrow, T.-F. Wong, and D. E. Moore (2006), Frictional strength of cuttings and core from SAFOD drillhole phases 1 and 2, *Geophys. Res. Lett.*, *33*, L23307, doi:10.1029/2006GL027626.

Toké, N. A., et al. (2011), Late Holocene slip rate of the San Andreas Fault and its accommodation by creep and moderate-magnitude earthquakes at Parkfield, California, *Geology*, *39*(3), 243–246.

Tse, S. T., and J. R. Rice (1986), Crustal earthquake instability in relation to the depth variation of frictional slip properties, *J. Geophys. Res.*, *91*, 9452–9472.

Waldhauser, F., W. L. Ellsworth, D. P. Schaff, and A. Cole (2004), Streaks, multiplets, and holes: High-resolution spatio-temporal behavior of Parkfield seismicity, *Geophys. Res. Lett.*, *31*, L18608, doi:10.1029/2004GL020649.

Wdowinski, S., Y. Bock, J. Zhang, P. Fang, and J. Genrich (1997), Southern California permanent GPS geodetic array: Spatial filtering of daily positions for estimating coseismic and postseismic displacements induced by the 1992 Lander earthquake, *J. Geophys. Res.*, *102*, 18,057–18,070.

Ziv, A. (2012), Inference of coseismic slip via joint inversion of GPS and aftershock data: The 2004 Parkfield example, *J. Geophys. Res.*, *117*, B03307, doi:10.1029/2011JB008400.